CERN
Esplanade des Particules 1
P.O. Box
1211 Geneva 23 - Switzerland

SY
Accelerator Systems

EDMS NO.	REV.	VALIDITY
3324712	**1.0**	**RELEASED**

REFERENCE
-

Based on template: EDMS 2375564

Date: 2025-07-04

Beam Synchrotron Radiation for the Longitudinal Density Monitor (BSRL) Error Analysis Report

ABSTRACT:

The Beam Synchrotron Radiation Longitudinal Density Monitor (BSRL) at the LHC leverages time-correlated single-photon counting to provide high-dynamic-range measurements of particle populations within each bunch in the LHC including monitoring of "ghost" and "satellite" bunches, which represent charge captured in nominally empty buckets, thereby enhancing the accuracy of luminosity calibration. As measurements from the BSRL are used in luminosity calibration it is vital that errors in its measurement are quantified and minimised where possible.

DOCUMENT PREPARED BY:	DOCUMENT TO BE CHECKED BY:	DOCUMENT TO BE APPROVED BY:
Alexander Jury – SY-BI Manuel Gonzalez Berges – SY-BI Stefano Mazzoni – SY-BI	Thibaut Lefevre – SY-BI	N/A

DOCUMENT SENT FOR INFORMATION TO:

[List of persons to whom the document is sent]

HISTORY OF CHANGES

REV. NO.	DATE	PAGES	DESCRIPTIONS OF THE CHANGES
0.1	2024-03-28	20	Creation of the document.

TABLE OF CONTENTS

1. Acronyms 4
2. Introduction 4
2.1 BSRL Components 5
2.1.1 Neutral Density (ND) filters 5
2.1.2 Wavelength dependent filter 5
2.1.3 Fibre optic cable 5
2.1.4 Detector 5
2.1.5 Time to Digital Converter (TDC) 5
2.2 Satellite and Ghost Bunches 6
3. Counting Errors 6
3.1 Dead time and pile up 6
3.1.1 Theory of dead time and pile up 7
3.1.2 Correcting for dead time and pile up 8
3.1.3 Measuring availability function 9
3.1.4 Error analysis 11
3.1.5 Results 11
3.2 After-pulsing 12
3.2.1 Theory of after-pulsing 12
3.2.2 Measuring after-pulsing 12
3.2.3 Experiment to define upper limit on after-pulsing 12
3.3 Background 14
3.3.1 Background correction 14
3.3.2 Background error 16
3.4 Beam Loss 17
3.4.1 Theory of cross-talk 17
3.4.1.1 Historical example 17
4. Timing errors 18
4.1 Timing source 18
4.2 Time to Digital Converter (TDC) 19
4.3 Dispersion within optical components 20
4.3.1 Measurement of dispersion 20

1. Acronyms

BSRL - Beam Synchrotron Radiation for the Longitudinal Density Monitor

SR - Synchrotron Radiation

HPM - Hybrid Photo-Multiplier

TDC - Time-to-Digital Converter

AD - Avalanche Diode

LHC - Large Hadron Collide

2. Introduction

The Beam Synchrotron Radiation Longitudinal Density Monitor (BSRL) is a non-invasive diagnostic tool that uses single photon counting of synchrotron radiation (SR) to measure the longitudinal distribution of protons or ions over many turns in the LHC [1].

The SR used by the BSRL is produced as the beams pass through a bending magnet or a purpose built superconducting undulator. This light is then extracted through fibre-optic cables. A range of neutral density filters is used to control the intensity before being detected by a hybrid photo-multiplier, capable of detecting individual photons.

Photon counts are given timestamps relative to the start of the turn, over many turns, to produce a histogram. From this, the relative populations within each RF bucket can be inferred. The longer the integration time the larger the dynamic range.

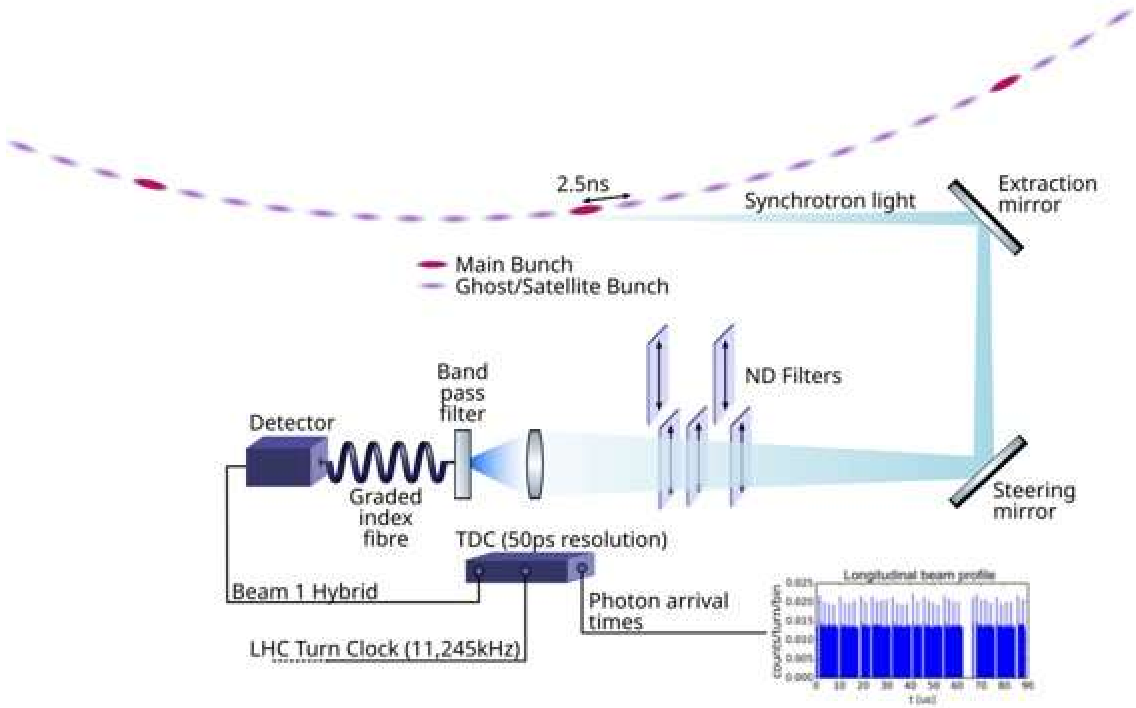

Figure 1 — Diagrammatic overview of the BSRL.

2.1 BSRL Components

2.1.1 Neutral Density (ND) filters

ND filters are used to control the rate at which photons are detected. Over the course of the fill, the intensity of the SR will vary over several orders of magnitude and the probability of detection per filled bunch per turn must be kept low to reduce the impact of dead-time. See Section 3.3.

2.1.2 Wavelength dependent filter

A 532 nm ± 10 nm (FWHM) bandpass filter is used to reduce the chromatic dispersion in subsequent optical components.

2.1.3 Fibre optic cable

The (Hybrid Photo-Multiplier) HPM is situated in the gantry to protect it from the radiation within the tunnel. See Section 3.3.

The fibre optic cables used are 50m long graded index MMC-Gvis/NIR-62.5-NA027-3-XPC-1500 produced by Schäfter and Kirchhoff.

Dispersion within the fibre is examined in Section 3.

2.1.4 Detector

The main component of the BSRL is a hybrid photo-multiplier (PicoQuant PMA 06) capable of single photon counting. This combines a traditional photo-multiplier tube and an avalanche diode (AD).

A photon incident on a photo cathode causes the liberation of an electron by the photoelectric effect. This electron is then accelerated in a vacuum tube by an electric potential towards the AD. Its collision with the AD causes the production of many electron hole pairs.

The AD is held in reverse-bias, close to the break down so that the minority carriers of the electron hole pairs generated in the previous stage gain more energy from the electric field, which in turn allows for the creation of more electron hole pair carriers. This process is the avalanche from which the AD takes its name.

The HPM is subject to several sources of error including dead time, after-pulsing and dark counts all examined in Section 3.

2.1.5 Time to Digital Converter (TDC)

The TDC assigns a time stamp relative to the start of the turn. At the time of writing this note, the TDC used in the LHC is an Acquiris TC890 (also called Agilent U1051A) and has 50 ps resolution and 14 ns deadtime.

2.2 Satellite and Ghost Bunches

Not every RF bucket in the LHC is intended to be filled. The RF at the LHC's operating energy has a period of 2.5 ns however the minimum distance between filled bunches is 25 ns.

For most purposes only the filled bunches are of interest. We introduce the concept of an RF slot, a set of 10 buckets arranged as can be seen in Figure 2. Charges in the 9 "nominally empty" buckets surrounding a filled bucket are referred to as "Satellites".

In addition, many slots are also left unfilled. Charge within these unfilled slots are referred to as "Ghosts".

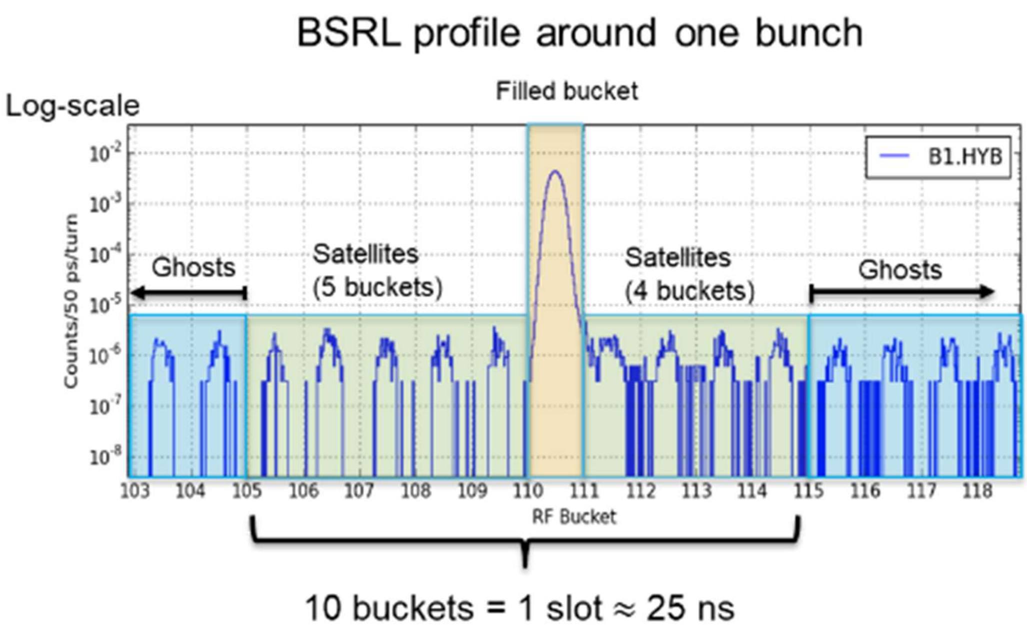

Figure 2 — Example of one RF slot, highlighting the definitions of filled, ghost and satellite buckets.

3. Counting Errors

Due to physical limitations of the detector and the time to digital converter not every photon present at the detector will result in a count, and therefore a loss of true counts will happen. Equally due to dark counting, after-pulsing and beam losses it is possible to have counts where there is no photon.

In this section these errors will be introduced and methods for their analysis examined and where possible the values of such effects will be quantified.

3.1 Dead time and pile up

The HPM relies on an avalanche gain. This avalanche process has a certain duration. After the arrival of a photon the HPM will be unable to detect any further photons for a limited period of time, as is illustrated in Figure 3.

The probability the detector is available to detect a new photon recovers gradually over a period t_{dead} of several nanoseconds, as can be seen in Figure 5. This is the dead time.

The TDC is only able to give time information to a precision of 50 ps. If multiple photons arrive in this period there will only be one count. This is referred to as pile up.

3.1.1 Theory of dead time and pile up

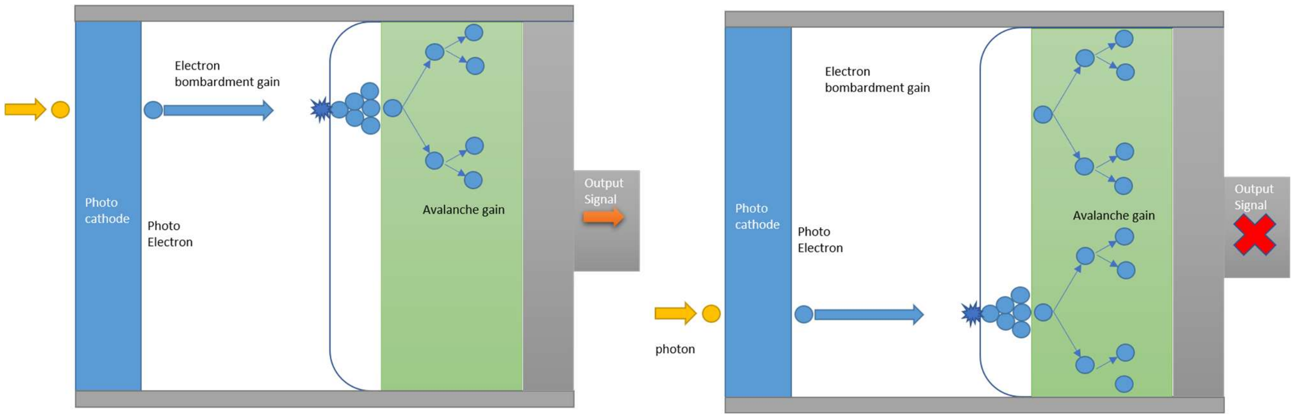

Figure 3 — Illustration of dead time in the HPM. Left: a photon is incident on the cathode and begins an avalanche process within the AD; Right: a second photon arrival $t < t_{dead}$ later and cannot be detected.

As the combined dead time of the HPM and TDC is greater than a typical bunch width there can be a maximum of one count per bunch per turn. Any other photons produced by a bunch will be missed. This causes a distortion in the measured distribution as photons produced by particles at the beginning of a bunch are more likely to be detected than those at the end. See Figure 4.

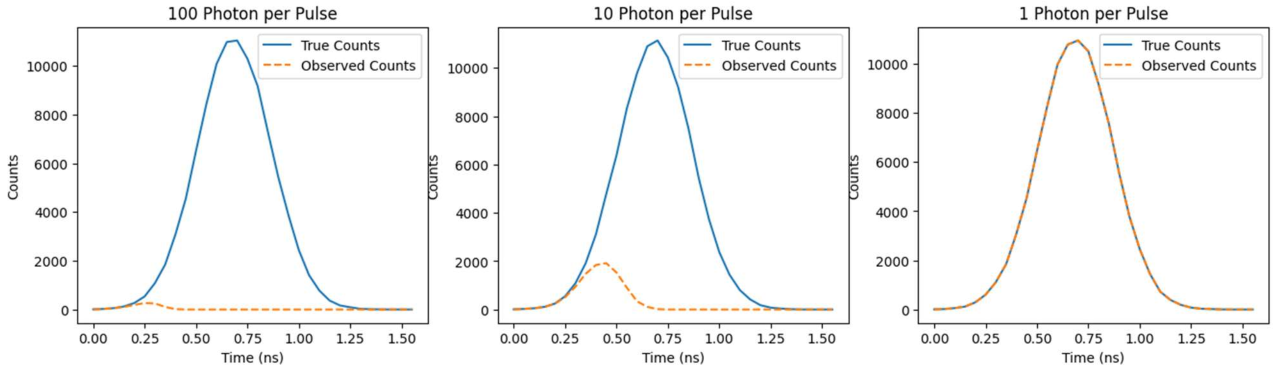

Figure 4 — Monte Carlo simulation of the effect of dead time on a histogram with bin size of 25 ps. Photon pulses are Gaussian with 89 ps standard deviation width and mean count rates of: (from left to right) 100 counts per pulse for 10^3 turns, 10 counts per pulse 10^4 turns, 1 count per pulse for 10^5 turns, total photons in simulation kept to 10^5.

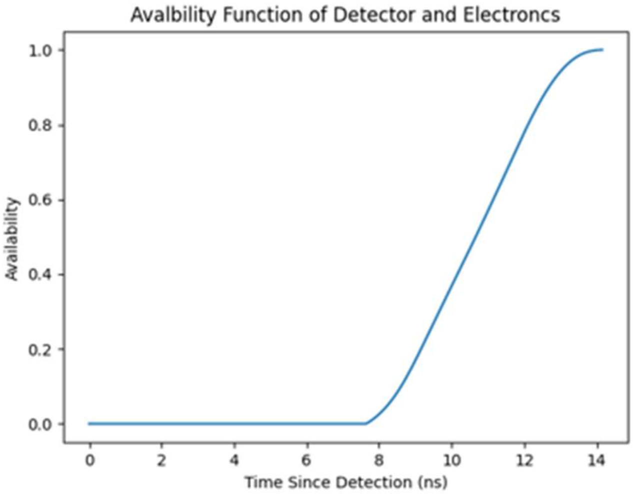

Figure 5 — Availability against time after detection
of the Acquiris TC890TDC and (PicoQuant PMA 06)Detector

3.1.2 Correcting for dead time and pile up

Assume that the of photons produced by particles in bin i per turn is drawn from a poison distribution distribution with mean λ_i

Then the probability of k photons being associated with bin i is

$$P(n_{pho} = k) = \frac{\lambda_i^k e^{-\lambda_i}}{k!} \tag{1}$$

The true mean is distorted by detector artifacts (pile up and deadtime)

First assume that only 1 photon per bin per turn can be detected (pile up)

The probability of a count per turn in bin i $\tilde{c_i}$ is then given by

$$\tilde{c_i} = P(n_{photo} > 0) = 1 - P(n_{photo} = 0) \tag{2}$$

Combining equations (1) and (2)

$$\tilde{c_i} = 1 - e^{-\lambda_i} \tag{3}$$

Now due to dead time in the detector there is some probability the detector will be available in bin i h_i

$$c_i = h_i \tilde{c_i} = h_i\left(1 - e^{-\lambda_i}\right) \tag{4}$$

Making λ_i the subject

$$\lambda_i = -\ln\left(1 - \frac{c_i}{h_i}\right) \tag{5}$$

We now must find h_i, however it is conceptually easier to find the probability the detector is unavailable. This is $1 - h_i$.

Let $\tau_{deadtime}$ be the number of bins it takes for the detector availability to return to 1 then $1 - h_i$ is the product of two factors:

1. The probability that there was a count to $\tau_{deadtime}$ bins before i

$$\sum_{j=i-\tau_{deadtime}}^{j=i} c_j \tag{6}$$

2. And the probability of a count at j causing the detector to be unavailable at i

$$(1 - S_{i-j}) \tag{7}$$

$$1 - h_i = \sum_{j=i-\tau_{deadtime}}^{j=i} c_j(1 - S_{i-j}) \tag{8}$$

As the detector is available before the count and after deadtime $(1 - S_{i-j}) = 0$ outside of this region and equation (8) can be rewritten as

$$1 - h_i = \sum_{j=-\infty}^{j=\infty} c_j(1 - S_{i-j}) \tag{9}$$

The right-hand side of equation is the definition of discrete convolution so

$$1 - h_i = c_i \otimes (1 - S_i) \tag{10}$$

Where $\otimes$ represents discrete convolution

Rearranging to make h_i the subject of the equation

$$h_i = 1 - c_i \otimes (1 - S_i) \tag{11}$$

combining equations (5) and (11) we recover the underlying distribution

$$\lambda_i = -\ln\left(1 - \frac{c_i}{1 - c_i \otimes (1 - S_i)}\right)$$

3.1.3 Measuring availability function

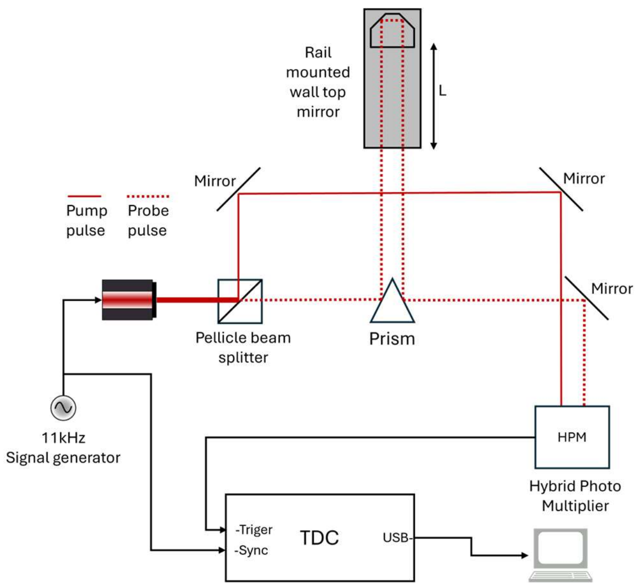

Figure 6 — Lab setup to measure the availability function of the Hybrid Photo-Multiplier and Time-to-Digital Converter

The availability function S used in the last two sections must be measured experimentally, this is done by generating two pulses of photons with a variable time delay τ. The first pulse (pump) is intended to put the detector into dead time, then the second pulse (probe) will be detected only if the detector is available.

The probe pulse is also measured separately without the pump to act as a reference.

Let M, H and H_r be the peak number of counts of the pump, probe and reference pulses, then by dividing these quantities by the total number of pulses that were measured we get m, h and h_r, the probability of detecting a count in the pump, probe and reference pulses, respectively.

h is dependent on whether there was a count detected in the pump pulse. If no photon was detected in the pump pulse, then for that turn $h = h_r$. However, if there is a detection in the pump pulse then $h = S(\tau)h_r$. Putting this together we get

$$h = mh_r + (1-m)S(\tau)h_r \tag{12}$$

Making $S(\tau)$ the subject

$$S(\tau) = \frac{1}{m}\left(\frac{h}{h_r} - (1-m)\right) \tag{13}$$

in this case, τ will be generated by an optical delay line as shown in Figure 6, $\tau = \frac{L}{c}$ where c is the speed of light.

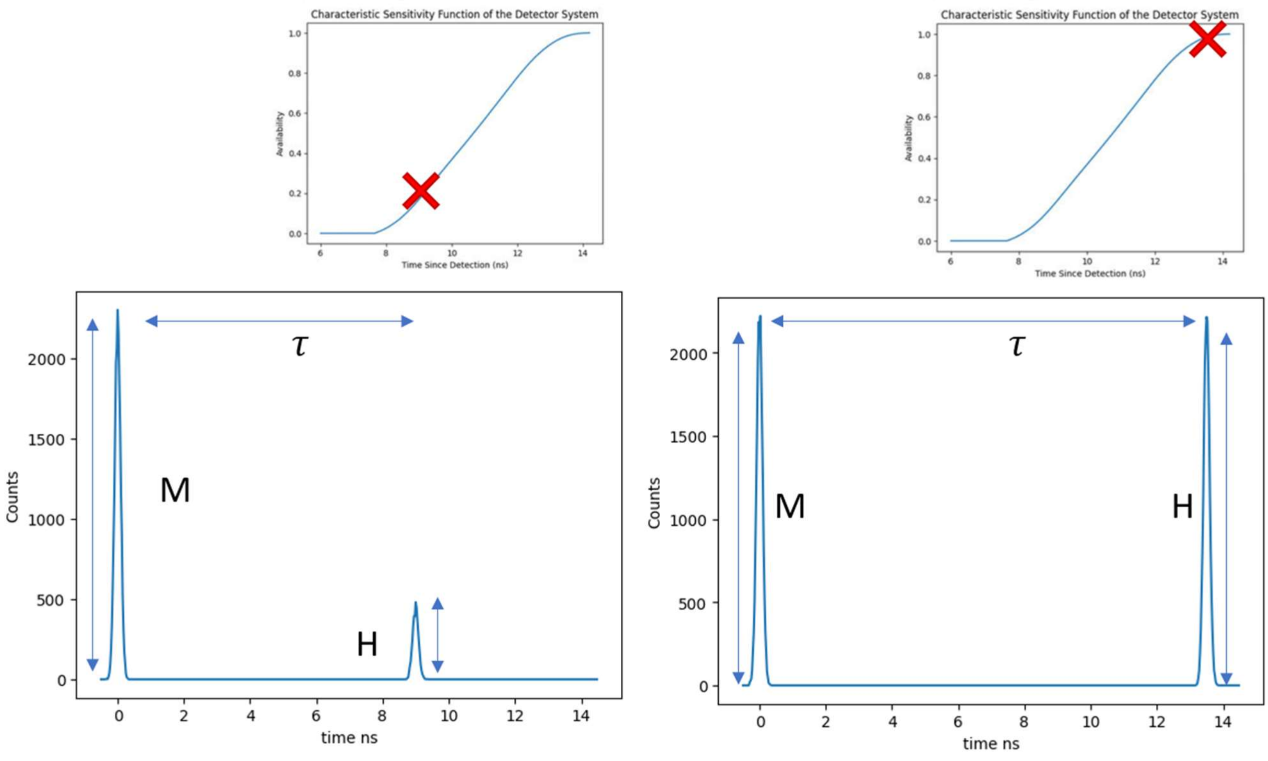

Figure 7 — Measurement of two points on the availability function

3.1.4 Error analysis

Due to random nature of counts, there will be inherent uncertainties in the heights of the peaks. This uncertainty diminishes with the number of counts and is given by

$$\delta N = \frac{1}{\sqrt{N}} \tag{14}$$

With uncertainties in the height of the pump, the probe and the reference peaks then the error in the in availability $\delta S = \sqrt{(\delta M)^2 + (\delta h)^2 + (\delta h_r)^2}$.

3.1.5 Results

The CAEN Mod. V1290-VX1290 A/N, 32/16 Ch. Multihit TDC and the PicoQuant PMA 06 hybrid photo multiplier were tested as described in this chapter and found to have a dead time of 6.1 ns which was in line with the manufacturer specification ~5 ns.

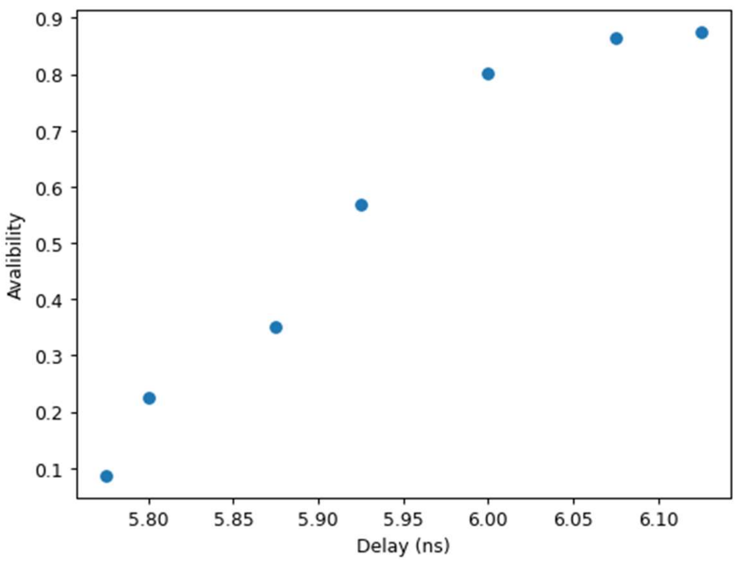

Figure 7a — Availability function CAEN Mod. V1290-VX1290 TDC and the PicoQuant PMA 06 hybrid photo multiplier

Further tests into the CAEN TDC were discontinued as it was deemed unsuitable for reasons beyond the scope of this document.

Ultimately the PicoQuant MultiHarp 150 was selected as the new TDC. The manufacturer lists the dead time of this card as 650 ps. This makes the optical setup described in Figure 6 less desirable due to the extreme precision required in positioning the wall top mirror.

A new experimental setup with multiple laser heads and an electrically generated delay is underway and will follow in a separate document.

3.2 After-pulsing

An after-pulse is a false count (in the absence of a photon) that is triggered by a true count sometime before.

3.2.1 Theory of after-pulsing

There are several possible sources of after-pulsing.

While the detector is undergoing a breakdown, it is possible for charge carriers to become trapped on the wrong side of the junction. These can be freed by thermal excitation at some random time later and cause a new avalanche.

Another source of after-pulsing is back-scattering. Electrons striking the AD can be reflected back; however, the voltage across this section of the detector slows these electrons before accelerating them back towards the AD to strike it for a second time.

It is also possible that, in the bombardment, an electron strikes a residual gas molecule producing a slowly drifting ion that arrives at the cathode sometime later.

3.2.2 Measuring after-pulsing

Measuring after-pulsing can be carried out by using a pulsed laser source, ensuring that the period between pulses is sufficiently long that all after-pulses have occurred before the next pulse.

3.2.3 Experiment to define upper limit on after-pulsing

In the optics lab, the detector response of the HPM and the TDC to a pulsed diode laser was measured and shows after-pulsing in the region 7-23 ns and 50-60 ns as can be seen in Figure 8.

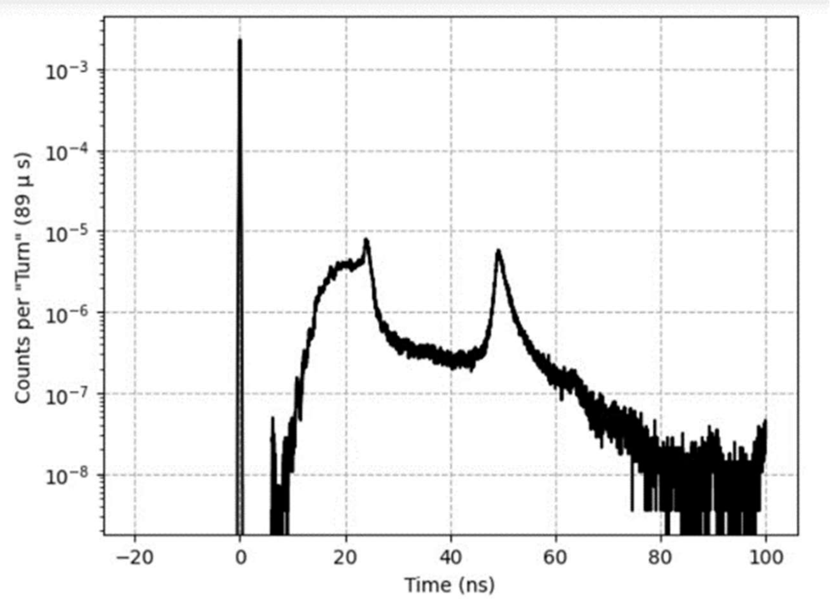

Figure 8 — The response of a system with a HPM (PicoQuant PMA Hybrid Series PMA Hybrid Series) and a TDC (Acquiris TC890) to a laser pulse of 11kHz over 5 minutes shows after-pulsing like behaviour.

As discussed in Section 3, multiple photons can cause a single count if they arrive close in time, however each of these photons has some probability of causing an after-pulse.

This has made measuring the absolute probability of an after-pulse challenging.

After-pulsing is not immediately obvious in the raw histogram produced by the BSRL during LHC physics operation as there are bunches overlapping the after-pulsing periods.

However, if bunches are well spaced (> 60 ns, 24 buckets) and total counts in the histogram are sufficiently high (> 10^6) after-pulsing becomes apparent, as is the case in Figure 9.

It is also possible to reconstruct after-pulsing in data from Van der Meer scans fills by summing the regions around bunches due to the large separation between bunches.

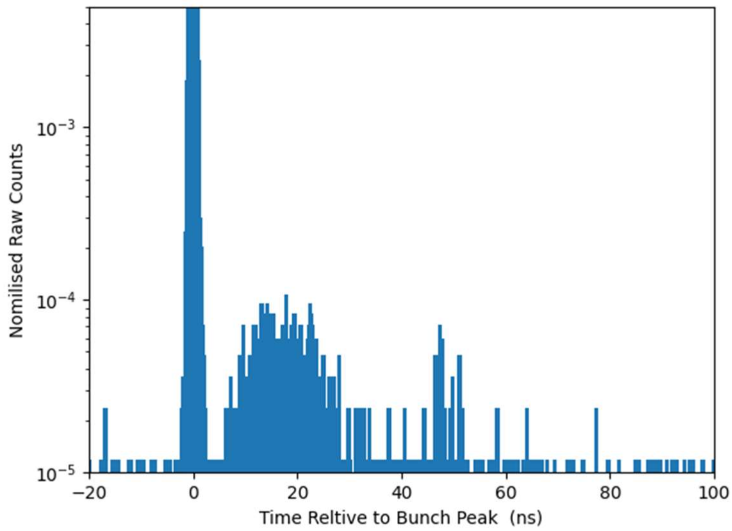

Figure 9 — Normalised counts around a bunch in fill 9352. Due to the high number of counts in the bunch and lack of surrounding bunches after-pulsing is clearly visible.

After-pulsing is currently being corrected by the background correction algorithm discussed in Section 3. The results of the algorithm on after-pulsing can be seen in Figure 10.

The bucket at position 19 after each bunch is not well corrected and is labelled as invalid, and for further calculations such as ghost and satellite fractions its value will be replaced by the global average of all valid buckets of its type (filled, ghost, satellite) and parity (odd, even bucket number).

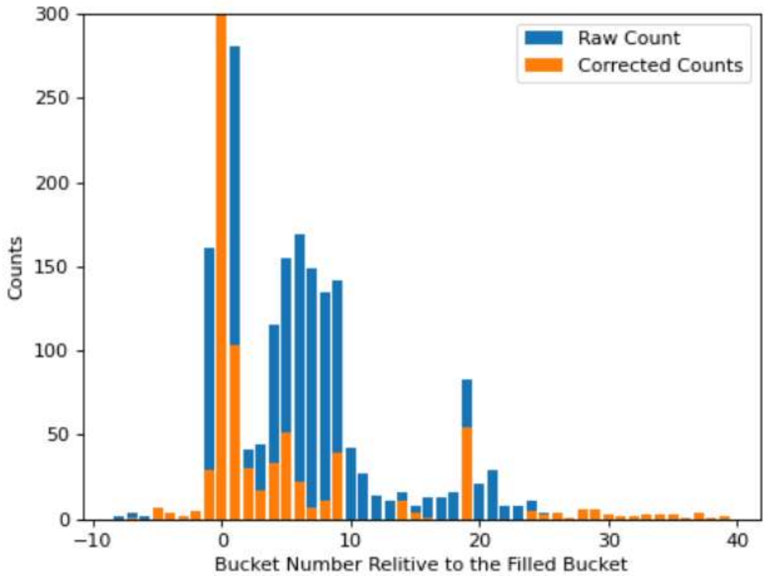

Figure 10 — The same data as see in Figure 9 this time having been grouped in to buckets by the BSRL data analysis. It can be seen that after-pulsing is greatly reduced by the background correction in all buckets, save for the 19th bucket after the bunch which is invalidated.

3.3 Background

Thermal and electrical noise in the system mean that even in the absence of light the detector will report counts. These "dark counts" are primarily thermal in origin [2]. To reduce dark counts the HPM uses active temperature stabilisation.

3.3.1 Background correction

To correct the histogram for dark counting and after-pulsing, an estimate of the background is made by considering these counts within the separatrix of the local RF buckets, where no particles can reside for many turns, so the majority of counts are due to background.

Each RF bucket is separated into sections; a centre region nominally of thirty-nine 50 ps bins, and two edge regions, each nominally of five 50 ps bins, and two buffer regions in between of 2.5 bins each as can be seen in Figure 11. The charge contained in the whole bucket is q_{tot}, in the edge is q_{edge}, and in the central region is q_{cent}

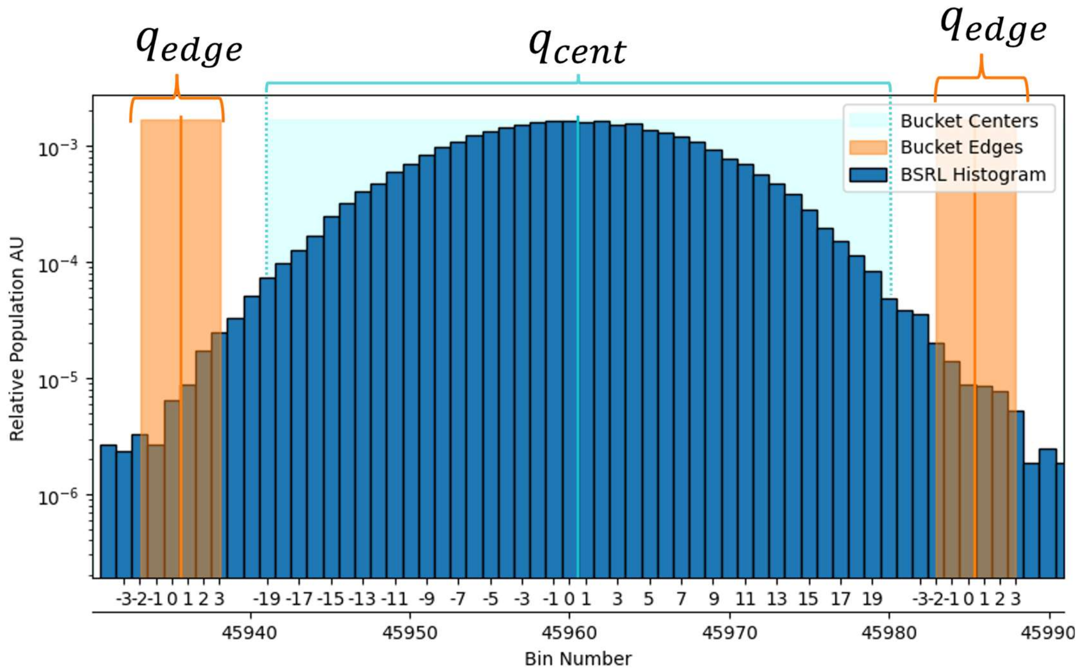

Figure 11 — Section of histogram around one filled bunch shows the regions of q_{cent} and q_{edge}

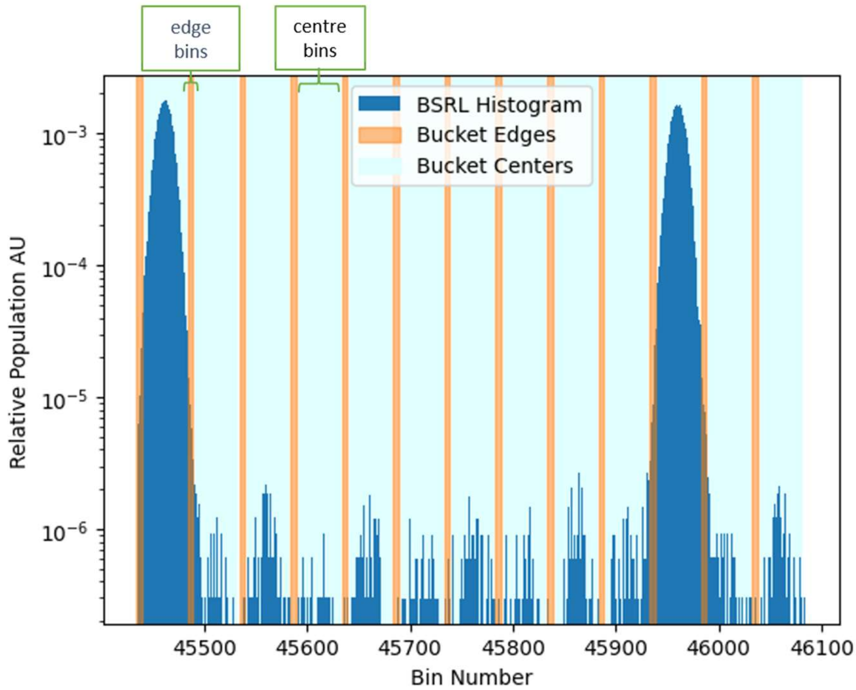

.

Figure 12 — Example of histogram being separated into bucket centres and bucket edges.

It is also important to note that due to bucket width not being an integer number of bins it is common for the regions of q_{cent} and q_{edge} to contain only fractions of a bin.

Due to timing errors, discussed further in Section 3, there is some probability that counts from the core of a bucket will be misattributed to the bucket edges. Because of the high occupancy, even the small fraction of misplaced counts dominates the true background. For this reason, the edges of filled buckets are not used to determine background.

A background estimate is calculated for each bucket by averaging over a moving window of a specified number of buckets (currently set to 3). This is shown in Figure 13.

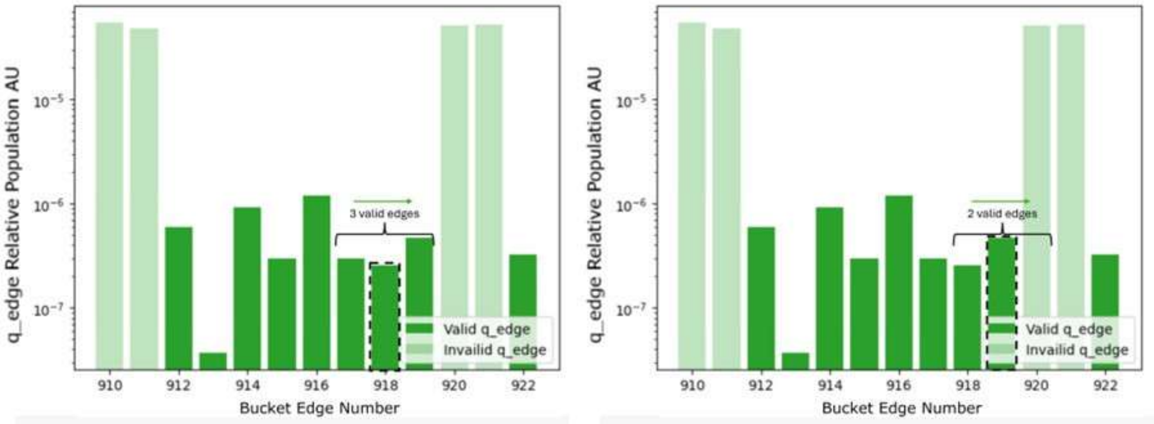

Figure 13 — Example of calculating $q_{baseline}$. Bucket edges 910 to 922. Note that the edges of the filled bucket 910, 911, 920, 921 are more than two orders of magnitude greater than the other edges. The sliding window shows how the baseline is calculated for each bucket.

$$q_{baseline} = \frac{\sum_i^{n_{valid}} q_{edge}}{n_{valid}} r \tag{15}$$

where r is the relative sizes of the centre region to the edge region in the nominal case $r = \frac{39}{5}$ and n_{valid} is the number of valid bucket edges within the sliding window.

The averaged bucket edges are now subtracted from the bucket centres to give the bunched charge, $q_{bunched}$

$q_{bunched} = q_{cent} - q_{baseline}$

If no valid bucket edges are present within the window,

then the window size is increased until there is at least one valid bucket edge for each RF bucket.

3.3.2 Background error

q_{tot}, q_{edge}, and q_{cent} are the means of Poisson distributions (divided by the number of turns) when the number of counts k is low the normal approximation is not appropriate and their confidence intervals can be found using Byar's method [3].

$$k_{lower} = k\left(1 - \frac{9}{k} - \frac{z_{\alpha/2}}{3\sqrt{k}}\right)^3$$

$$k_{upper} = (k+1)\left(1 - \frac{9}{k+1} - \frac{z_{\alpha/2}}{3\sqrt{k+1}}\right)^3 \tag{16}$$

$$k_{lower} \leq \langle k \rangle \leq k_{upper}$$

Where $\langle k \rangle$ is the distribution mean and α is determined by the desired level of confidence.

For example, if the 68% confidence interval is chosen i.e. where 68% of observations will be within the interval k_{lower} to k_{upper} then $\alpha = 1 - 0.68 = 0.32$ then $\frac{\alpha}{2} = 0.16$ and $z_{\alpha/2}$ is the standard normal deviate.

As the dark counting rate should be independent of the bucket the uncertainty in $q_{baseline}$ is repressed by its standard deviation $\sigma_{baseline}$.

Then the confidence interval for q_{bu} is

$$q_{bunched,lower} = q_{bunched} - \sqrt{\left(q_{cent} - q_{cent,lower}\right)^2 + \sigma_{baseline}} \tag{17}$$

$$\sigma_{q_{bunch}} = \sqrt{q_{bunched} - q_{bunched,upper}} \tag{18}$$

3.4 Beam Loss

Particles are lost from the LHC beams causing an increased background within the tunnel.

3.4.1 Theory of cross-talk

Particles lost (and the secondary particles they create) from Beam 1 can strike the detector of Beam 2. This would cause counts to be registered in the same manner as photo-electrons.

This produces a much weaker "echo" of Beam 1's bunch structure in Beam 2's signal.

This echo can only be seen in regions of Beam 2 with a low level of counts, as the signal from beam loss is drowned out in the statistical noise of the filled bucket. The same is true of particles lost from Beam 2 being detected by the detector of Beam 1. An example from 2015 can be seen in Figure 13.

3.4.1.1 Historical example

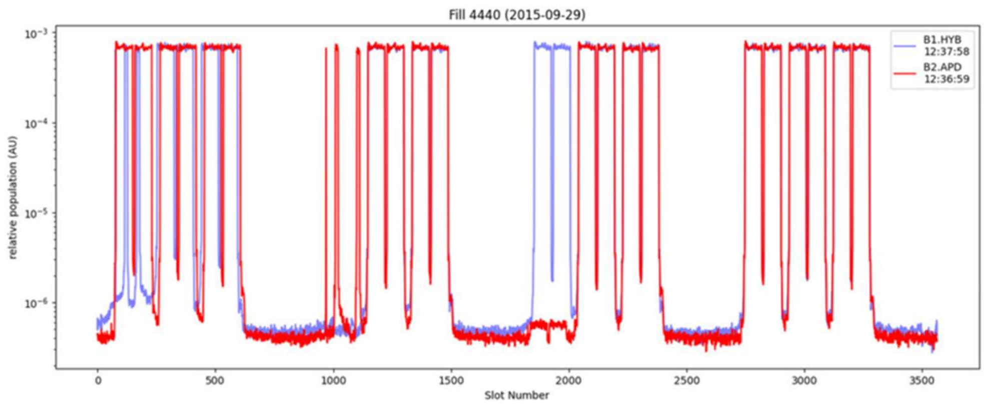

Figure 14 — Slot Histogram from LHC fill 4440. Signals due to beam loss can be seen in the region around slot 1000, where the shape of Beam 1 can be seen in Beam 2.

The evidence of beam loss striking the detectors lead to concerns of the longevity of the detector and so the detector was removed to a gantry in 2016. See Figure 15. This required the introduction of a fibre to transport the extracted photons.

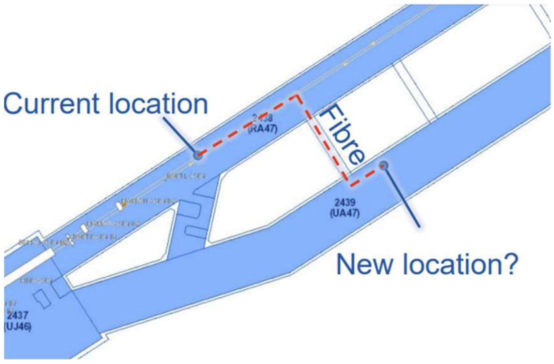

Figure 15 — Change of location carried out in 2016.

4. Timing errors

The labelling of counts in time is integral to the creation of the raw histogram.

Timing errors come from multiple components, for example the timing source, internal clock jitter and dispersion within the optical fibre. Each of these sources can be treated independently and so the total timing error is the quadratic sum of all sources.

4.1 Timing source

All timestamps produced by the BSRL are given relative to a reference marking the start of the turn, historically this signal was taken from the Beam Synchronous Timing (BST) which transmits timing information from the RF system to points all around LHC though kms of optical fibre.

The uncertainty in this timing is 1 ns peak to peak, or standard deviation of 300 ps. This has been obtained empirically.

This error was found to be the dominant timing error in the BSRL. The bunch lengths inferred from the BSRL histogram to those measured had a Gaussian blurring applied. The best fit is found when the sigma of this Gaussian is 300 ps, which matches the BST turn clock uncertainty.

To reduce this timing error and to profit from the relative closeness of the RF system, the BSRL can take timing signals directly from the RF system. This change was implemented in the 2023-2024 YETS.

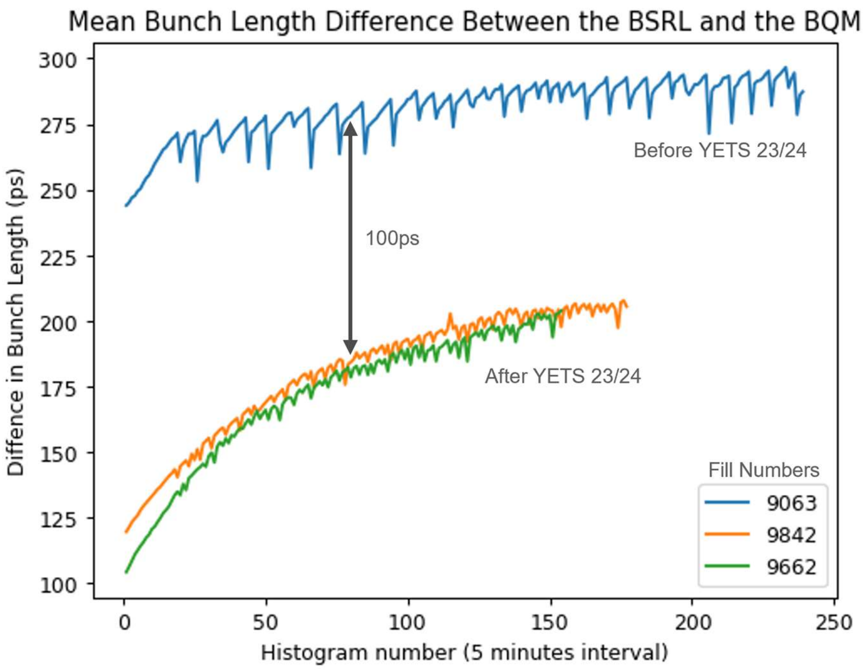

Figure 16. Difference in 4 sigma bunch length measurements from BSRL and BQM fills Before and after the change of timing reference

4.2 Time to Digital Converter (TDC)

The TDC used in the BSRL is the Acquiris TC890. The turn clock pulse is fed into the TDC as a start pulse. When a signal is received from the Detector, the TDC provides a timestamp of the time since the start pulse.

The error from the TDC, σ_{TDC}, is a combination of a number of factors

$$\sigma_{TDC} = \sqrt{(\sigma_{TimebaseError})^2 + (\sigma_{StartError})^2 + \left(\sigma_{StopError}\right)^2 + (\sigma_{FGI})^2} \tag{19}$$

where $\sigma_{TimebaseError}$ is the error contribution of the TDC reference clock, $\sigma_{StartError}$ and $\sigma_{StopError}$ are the errors in the detection of the start and stop signals. σ_{FGI} is the error contribution from the fine grained interpolator due to integral non-linearity and differential non-linearity effects in the analog to digital converter used to digitise edge signals.

For the TC890, $\sigma_{FGI} = 80\,ps$, while $\sigma_{TimebaseError}$ is given by

$$\sigma_{TimebaseError} = Measured\ \ time \times Clock\ Accuracy$$

where $Clock\ Accuracy$ is the stability of the 10 MHz reference clock which is 2 parts per million, and $Measured\ time$ is the actual time measured between the interval start hit and its stop hit.

$\sigma_{StartError}$ and $\sigma_{StopError}$ are themselves made up of two components, σ_{noise}, the error due to electronic noise, and σ_{level}, which is the error caused as a signal does not cross the trigger level instantaneously

$$\sigma_{noise} = \frac{2\sqrt{\left(E_{signal}^2\right) + \left(E_{input}^2\right)}}{S} \tag{20}$$

where E_{signal} is the root-mean-squared (RMS) noise value of the signal filtered by the input circuit of the TDC, $\mathrm{E}_{\mathrm{input}} \approx 15\,\mu\mathrm{V}$, E_{input} is the RMS input noise of the TDC and S is the input signal slew rate

$$\sigma_{level} = \frac{threshold\ error}{S} \tag{21}$$

$threshold\ error\ = 15\,mV$ for trigger stops with different slopes and/or different input channels.

4.3 Dispersion within optical components

With the expected reduction in timing error from taking start signals directly from the RF system we must now turn our attention to smaller timing errors such as that caused by the optical dispersion in the fibre that takes the photons from the tunnel to the gantry.

4.3.1 Measurement of dispersion

The exact length of the fibre optic cable has been measured in the 2024-2025 YETS and was found to be.

Beam	Length (m)	Estimate of Dispersion(ps) FWHM
B1	110.9	484.6
B2	122.5	535.3

The dispersion was estimated by modelling the fibre as pure fused silica and considering the $532 \pm 10\,nm$ wavelength range set by the bandpass filter, yielding a value of $437\,ps/nm\ km$ [4]

It is planned that the dispersion including higher order components will be measured in the lab in 2025.

From there we hope to be able to deconvolve in software the original signal from the dispersion this will make the histograms produced by the BSRL more accurate in turn make the correction for background after pulsing and dead time more effective

5. References

[1] A. Jeff, “A Longitudinal Density Monitor for the LHC”,Ph.D. dissertaion Liverpool, 2012.

[2] R. Paschotta, “Photon Counting,” 25 03 2007. [Online]. Available: {https://www.rp-photonics.com/photon_counting.html. [Accessed 25 03 2025].

[3] G. F. G. Z. Hon Keung Tony Ng, “Confidence interval estimating procedures for standardized incidence rates,” *Computational Statistics and Data Analysis,* vol. 52, no. 7, pp. 3501--3516, 2008.

[4] M. N. Polyanskiy, “Refractiveindex.info database of optical constants,” *Sci. Data,* vol. 11, no. 94, 2024.

[5] PicoQuant, “PMA Hybrid Series,” Berlin, 2024.

[6] Schäfter and Kirchhoff, “Multimode Fiber Cables MMC,” Schäfter and Kirchhoff, [Online]. Available: https://www.sukhamburg.com/products/fiberoptics/fibercable/mm.html. [Accessed 06 04 2025].

[7] Agilent Technologies, “USER MANUAL AGILENT ACQIRIS,” 2012.